Electrical Engineering and Computer Science Plan B Projects

2019

An Analysis on the Correlation Between Atmospheric Parameters and TOA Reflectance of Pseudo Invariant Calibration Sites (PICS)

Yugeen Chaulagain

South Dakota State University, chaulagain.yugeen@gmail.com

An Analysis on the Correlation Between Atmospheric Parameters and TOA Reflectance of

Pseudo Invariant Calibration Sites (PICS)

By

Yugeen Chaulagain

A research paper submitted in the partial fulfilment of the requirement for the

Master of Science

Major in Electrical Engineering

South Dakota State University

2019

TABLE OF CONTENTS

CHAPTER 1

INTRODUCTION

1.1 Significance of Calibration

The sensors onboard the Landsat series satellites have recorded numerous images of the Earth's surface since the beginning of the Landsat program in 1972. Each generation of sensor has been built with increased spectral, spatial, and radiometric resolution, leading to increased use of their imagery to study natural and human-induced changes to the planet. To ensure reliable information is derived from the image data, the sensors need to be accurately calibrated, both radiometrically and geometrically.

Radiometric calibration of satellite-based imaging sensors has been extensively studied, and can be absolute or relative in nature. Absolute radiometric calibration of an individual sensor provides gains and offsets used to convert raw image pixel values to accurate estimates of top-of-atmosphere (TOA) radiance and/or reflectance. Relative radiometric calibration determines factors applied to each detector's raw pixel values to equalize the detector's radiometric response.

The information required to perform radiometric calibration can be acquired from measurements obtained with sources onboard the sensor (e.g. solar diffuser panels, lamps, thermal blackbody sources, etc.), or from measurements derived directly from image data. Pseudo Invariant Calibration Sites (PICS), primarily located in desert or other arid regions, have demonstrated excellent potential as sources for image data used in radiometric calibration. They offer consistent temporal, spatial, and spectral stability to within 3% [1]. If PICS-based calibration results are compared with onboard calibration results, it can help to confirm whether any observed changes in radiometric response are due to changes to the sensor itself.

Several works were developed using PICS for trending of sensors gains, sensors cross-calibration, and, more recently, absolute calibration [2]. However, one issue that has not yet been addressed and studied thoroughly was the effects of the atmosphere on PICS. Water vapor, barometric pressure, ozone, and aerosols present in the atmosphere alter the amount of solar energy striking the Earth's surface through scattering and absorption processes that are wavelength dependent. For PICS, it has been estimated that up to a third of the total estimated uncertainty is due to uncorrected atmospheric effects [2]. As PICS are located in drier regions, the effects of atmospheric water vapor are generally minimized. However, the lower the temporal uncertainty of the site, the more important it is to understand its atmosphere.

1.2 Objective

The objective of this work is to understand and quantify the relationship(s) between atmospheric parameters and TOA reflectance. The analysis uses Landsat-7 ETM+ and Landsat-8 OLI images data acquired over the Algodones Dunes and a desert site near Wadi ad-Dawasir, Saudi Arabia. The analysis focuses on atmospheric water content and barometric pressure, as ground truth measurements of these quantities are likely to be readily available from relatively nearby weather stations. Section II of the paper discusses the methodology used in the analysis. Section III presents the analysis results. Finally, Section IV provides a summary and considers potential directions for future investigation.

1.3 Definition of Atmospheric Parameters Considered in the Paper

This section briefly defines the atmospheric parameters considered in this work: relative (and absolute) humidity, and atmospheric pressure. These parameters were chosen because they were the most readily available in the weather station data. Humidity was the selected parameter for characterization of the longer wavelength bands,

1.3.1 Relative Humidity

Relative humidity is defined as the ratio percentage of the water vapor pressure to the saturation water vapor pressure at the gas temperature (273° K) [3]:

$$RH = \frac{P_w}{P_{ws}} \times 100\% \tag{1}$$

where p_w and p_{ws} are the absolute water vapor pressure and saturation water vapor pressure in Pa, respectively. The saturation water vapor pressure is the maximum pressure possible by water vapor at a given temperature.

Relative humidity is a function of the ambient air temperature through p_{ws}:

$$p_{ws} = \frac{1}{T^{8.2}} \times \exp(77.345 + 0.0057 \times T - \frac{7235}{T}) \tag{2}$$

The absolute humidity is defined as the mass of water vapor in a given volume. It is also a function of the ambient air temperature.

$$AH = c \times \frac{p_w}{T} \tag{3}$$

where c = 2.16679 gK/J and T is the ambient air temperature in °K.

Relative humidity can be converted to absolute humidity as follows. First, solve equation (1) for p_w:

$$p_w = RH \times p_{ws} \tag{4a}$$

Then substitute (4a) into equation (3):

$$AH = c \times \frac{1}{T^{9.2}} \times RH \times \exp(77.345 + 0.0057 \times T - \frac{7235}{T}) \tag{4b}$$

1.3.2 Atmospheric Pressure (Barometric Pressure)

Atmospheric pressure, or barometric pressure, is the pressure produced by the combined weight of the gasses comprising the Earth's atmosphere. It is inversely proportional to elevation above

the Earth's surface (i.e. atmospheric pressure is lower at higher elevation). For the purposes of this work, atmospheric pressure is measured in inches of mercury (in. Hg).

Rayleigh scattering can be expressed as a linear function of atmospheric pressure [4]:

$$\tau_{Rayleigh} = k\frac{P}{P_0} \tag{5}$$

where P_0 is the standard atmospheric pressure at sea level (approximately 29.92 in Hg), and k represents a function of λ^{-4}. Since Rayleigh scattering is predominant at shorter wavelengths, it is expected that TOA reflectance at shorter wavelengths would be more affected by atmospheric pressure.

1.4 Relative Spectral Response of Landsat-7 ETM+ and Landsat-8 OLI

Figures 1a and 1b show the relative spectral responses (RSRs) for each band in the ETM+ and OLI. The OLI RSRs are narrower and exhibit less variability in response across the passband than the corresponding ETM+ RSRs. The OLI NIR band is shifted considerably towards the falling edge of the ETM+ NIR band, and the OLI SWIR1 band is shifted towards the rising edge of the ETM+ SWIR1 band. These changes to the OLI response were intended to reduce the sensitivity of these bands to water vapor absorption.

The OLI has 2 additional bands the ETM+ does not: a Coastal/Aerosol band (approximately 430 to 450 nm) and a Cirrus band (approximately 1360 to 1380 nm). The Coastal/Aerosol band is approximately centered on the rising edge of the ETM+ Blue band. As its name suggests, the Coastal/Aerosol band is intended to measure atmospheric aerosols, while the Cirrus band is intended to detect thin cirrus clouds. For the purposes of this work, the Cirrus band is not considered further.
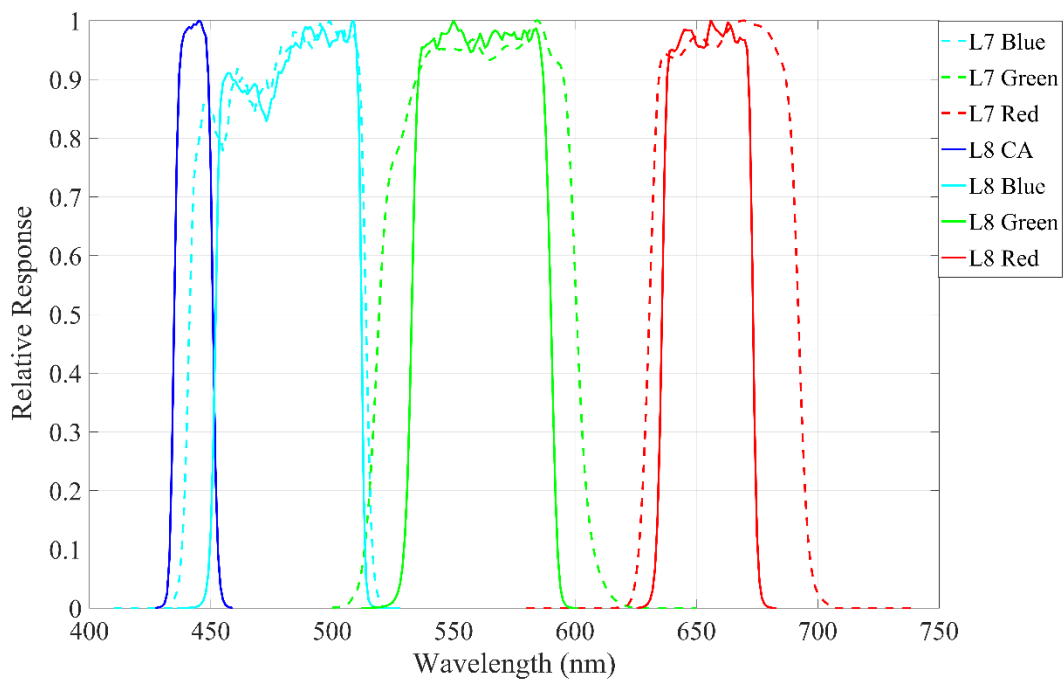
Figure 1a: ETM+ and OLI RSR for shorter wavelength bands.
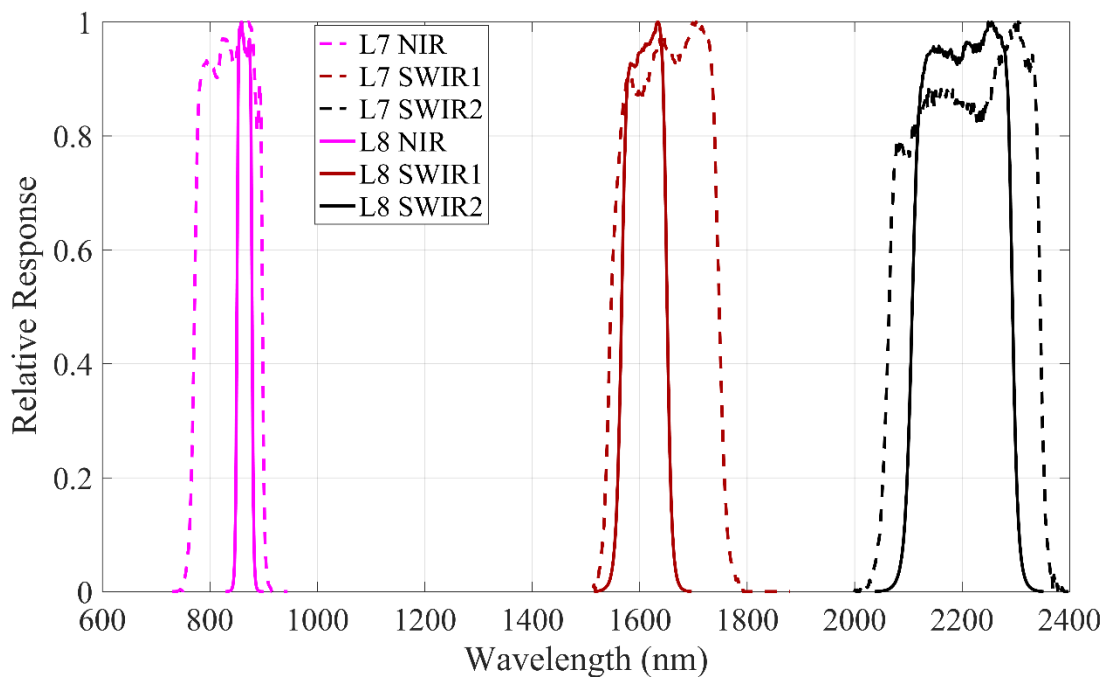
Figure 1b: ETM+ and OLI RSR for longer wavelength bands.

CHAPTER 2

METHODOLOGY

This chapter discusses the methodology used to perform the analysis, beginning with the procedure(s) used to select the test sites. The remainder of the chapter describes the characteristics of the selected sites and the procedures used to perform the analysis.

2.1 Site Selection

The following criteria were used to guide the target site selection process:

- The target(s) should be as bright as possible. Reflectance measurements from brighter targets have higher signal-to-noise ratios.

- The target(s) should exhibit low temporal and spatial uncertainty. This will help to ensure that any changes measured by the sensor represent changes in the sensor response only

- Atmospheric measurements should be available for the target(s), and should come from an operative weather station situated as close as possible to the target ROI. Atmospheric measurements from stations close to the ROI should better represent the "true" condition of the atmosphere over the ROI. There could be significant differences in atmospheric measurements between the two locations.

Initially, PICS target(s) were considered in order to meet the first two criteria. From the set of North African PICS studied by the Image Processing Laboratory, Libya-1 (WRS2 path/row 187/043), Libya-4 (WRS2 path/row 181/040), Niger-1 (WRS2 path/row 189/046), Niger-2 (WRS2 path/row 188/045), and Sudan-1 (WRS2 path/row 177/045) were chosen, as these demonstrated the most temporal and spatial stability. Unfortunately, co-incident atmospheric measurements

from a nearby weather station were not available for these sites. Two alternative sites were selected that had co-incident ground truth atmospheric measurements: (i) Algodones Dunes, CA (USA); and (ii) a site near the city of Wadi ad-Dawasir, Saudi Arabia. Both sites are described below.

2.1.1 Algodones Dunes

The Algodones Dunes (WRS-2 path/row 039/037), located near the U.S.-Mexico border, has been previously used for sensor absolute and cross calibrations [5]. Due to surface characteristic similarities with the Libya-4 PICS and its easier accessibility, it has been identified as a potential intercalibration site.
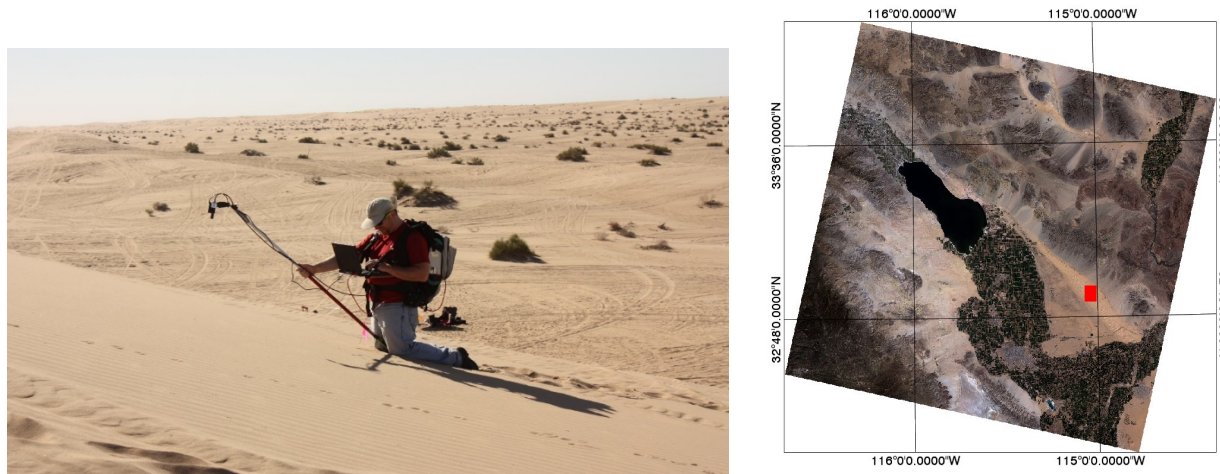
Figure 2: (a) Algodones Dunes, 2015 Image Processing Laboratory Field Campaign; (b) Landsat-8 OLI Image of Algodones Dunes. The solid red rectangle represents the optimal ROI.

The site itself consists of sparsely vegetated sand dunes (Figure 1) covering an area approximately 45 miles in length and 6 miles in width, running from northwest to southeast. The ROI containing the minimum spatial and temporal uncertainty was identified with techniques developed by the Image Processing Laboratory [6]. Co-incident measurements of relative humidity, ambient temperature, and barometric pressure were available through the Imperial County Airport weather station in Imperial CA, located approximately 30 miles from the selected ROI.

2.1.2 Wadi ad-Dawasir, Saudi Arabia

An additional site in southwestern Saudi Arabia within the Arabian Desert (WRS2 path/row 166/046) (Figure 2), near the city of Wadi ad-Dawasir, was selected based on initial identification through a global search as potential PICS [7] with an estimated temporal uncertainty within 3% across all bands.
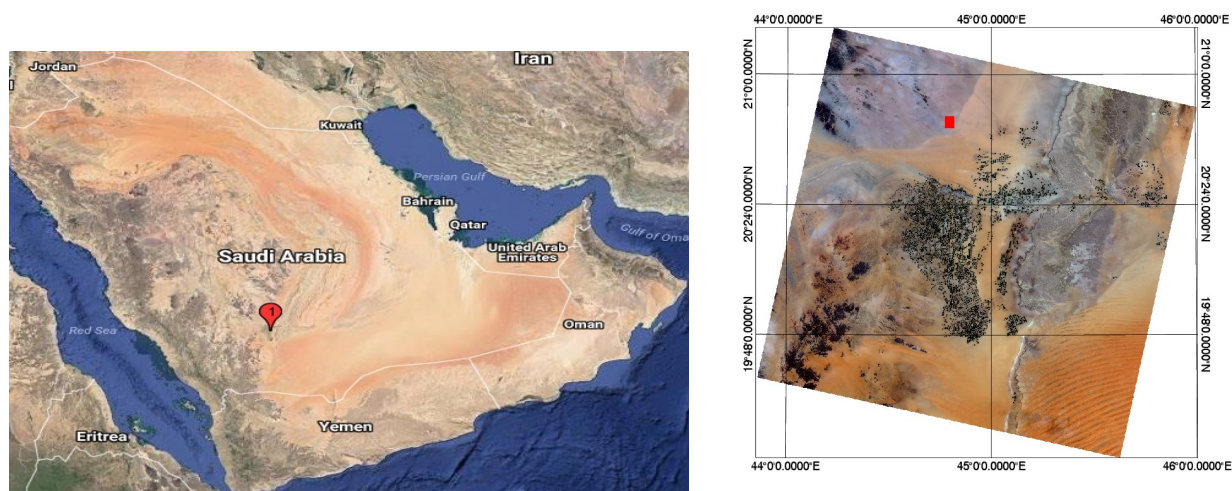
Figure 3: (a) Selected site near Wadi ad-Dawasir, Saudi Arabia (indicated by red marker); (b) Landsat-8 OLI Image of Wadi-ad-Dawasir, Saudi Arabia. The red rectangle represents a 40x40 ROI in a region identified as stable in the SWIR2 band.

The site is smaller in area than Algodones Dunes. It is located near the base of a rocky outcropping north of a significant area of irrigated agriculture. Co-incident atmospheric measurements were available from the Wadi ad-Dawasir Airport weather station, located approximately 35 miles from the selected ROI.

2.2 Analysis Methodology

2.2.1 Image Selection and Pre-processing

The data used to find the TOA reflectance over Algodones Dunes were 260 cloud-free images of Landsat-7 ETM+ from 1999 to 2017, and 68 Landsat-8 OLI images from 2013 to 2017 selected from the Image Processing Laboratory archive of collection 1 image data. Similarly, 79 cloud-free

Landsat-8 OLI images from 2013 to 2017 were selected for the Wadi ad-Dawasir site; ETM+ image data were not used in the analysis of this site as there was insufficient co-incident weather station data available.

The Image Processing Laboratory archived image data were originally processed at the USGS EROS Data Center with the Landsat Product Generation System (LPGS) [8] to correct radiometric and geometric artifacts. The corresponding calibrated pixel values were then converted to TOA reflectances as follows [9]:

$$\rho_{TOA} = \frac{1}{\cos\theta_z}(M_\rho Q_{cal} + A_\rho) \tag{6}$$

where M_ρ and A_ρ are band-specific, reflectance-based multiplicative and additive scaling factors given in the product metadata, Q_{cal} is the calibrated DN value for the given pixel, and θ_z is the solar zenith angle for the given pixel, obtained from a solar angle "image" band generated for the particular image product.

2.2.2 Deriving the Relationships Between TOA Reflectance and Atmospheric Parameter

Once the TOA reflectance summary statistics (i.e. mean, standard deviation, and temporal uncertainty) were obtained from the selected ROIs at the target site and the corresponding set of atmospheric parameter measurements were identified, the following steps were performed to identify any relationships between TOA reflectance and atmospheric parameters. First, least-squares linear regressions were fit to the TOA reflectance data:

$$\rho_{TOA} = \beta_0 + \beta_1 \times param \tag{7}$$

where β_0 and β_1 are the intercept and slope coefficients and *param* is the atmospheric parameter of interest (in this work, absolute humidity and barometric pressure). The slope is represented in units of reflectance / unit of atmospheric parameter.

The significance of the regression slopes was then tested using a two-sided hypothesis test at the 0.05 significance level. If the p-value of the test was greater than 0.05, there was insufficient evidence to reject the null hypothesis of zero slope. If the p-value of the test was less than or equal to 0.05, there was sufficient evidence to reject the null hypothesis and conclude a (statistically significant, at least) relationship between TOA reflectance and the given atmospheric parameter existed.

For those bands exhibiting sufficient statistical evidence to reject the null hypothesis of zero slope, additional processing was performed to determine whether a linear function of atmospheric parameter adequately accounted for the observed TOA reflectance behavior. This additional processing is described in the following sections.

2.2.3 Consideration of Higher-Order and/or Nonlinear Atmospheric Parameter Models

In addition to linear functions of a single atmospheric parameter, higher-order and nonlinear functions of a single atmospheric parameter were also considered. For each model tested, the R^2 value was calculated to estimate the goodness of the model fit. The model having the highest R^2 value was selected as the "optimal" model, and used to normalize the initial TOA reflectance data as follows:

$$\rho_{corr} = \frac{\rho_{obs}}{\rho_{model}} \times \overline{\rho_{obs}} \tag{8}$$

where ρ_{obs} is the observed TOA reflectance, ρ_{model} is the predicted TOA reflectance accounting for the given atmospheric parameter(s), and $\overline{\rho_{obs}}$ is the temporal mean of the observed TOA reflectance. The normalized TOA reflectances were then replotted to check whether the temporal uncertainty (i.e. the "spread" in the set of data points) was reduced after the correction.

2.2.4   BRDF Normalization

Typical analyses of desert site image data have used large areas (on the order of several hundred km^2) in order to minimize BRDF effects [10]. Since the optimal regions used in this work tend to be much smaller in area, BRDF effects due to variation in solar position and/or sensor viewing position throughout the year cannot be ignored.

For the Algodones Dunes site, a two-angle quadratic BRDF model was used:

$$\rho_{BRDF} = \beta_0 + \beta_1 x_1^2 + \beta_2 y_1^2 + \beta_3 x_1 y_1 \tag{9}$$

For the Wadi ad-Dawasir site, a four-angle linear BRDF model was used:

$$\rho_{BRDF} = \beta_0 + \beta_1 x_1 + \beta_2 y_1 + \beta_3 x_2 + \beta_4 y_2 \tag{10}$$

For both models, x_1, x_2, y_1, and y_2 are the plane Cartesian coordinate values transformed from the solar position zenith/azimuth angles (SZA, SAA) and sensor viewing zenith/azimuth angles (VZA, VAA) based in a spherical coordinate system.

$$x_1 = \sin(SZA)\cos(SAA) \tag{11a}$$

$$y_1 = \sin(SZA)\sin(SAA) \tag{11b}$$

$$x_2 = \sin(VZA)\cos(VAA) \tag{11c}$$

$$y_2 = \sin(VZA)\sin(VAA) \tag{11d}$$

CHAPTER 3

RESULTS

This chapter presents the results of the analysis methodology given in the previous chapter. Results for normalization using the "optimal" atmospheric parameter model are presented only for those bands demonstrating a statistically significant linear relationship between TOA reflectance and the atmospheric parameter of interest. The results for each sensor are presented according to site; the results for absolute humidity are presented first, followed by the results for barometric pressure.

3.1 Algodones Dunes

3.1.1 Relationship Between TOA Reflectance and Absolute Humidity—Landsat 7 ETM+ NIR Band:

Figure 3 shows the relationship between TOA reflectance and absolute humidity for the NIR band. The slope of the regression line was found to be strongly statistically significant (p-value = approximately 6.83×10^{-23} at the 0.05 significance level) and, as expected, indicated a negative relationship between TOA reflectance and absolute humidity. The linear model accounted for approximately 31.4% of the variability in the TOA reflectance.

The optimal atmospheric parameter model was found to be the initial linear model:

$$\rho_{model} = 0.4071 - 0.001318 \times AH \tag{12}$$

Figure 4 shows the resulting normalization provided with this model. The figure indicates that after normalization the overall "spread" in the data was reduced. The reflectances of a few data points (e.g. the early 2006 acquisition), however, appeared to be reduced further away from the TOA reflectance mean. Table 1 shows the resulting statistics before and after normalization with the atmospheric model. Clearly, the temporal uncertainty was reduced by the normalization.

a= 0.4071 b= -0.001318 R-sq= 0.3139 P-value= 6.825e-23

Figure 3: Linear relationship between NIR TOA Reflectance and Absolute Humidity.

Figure 4: NIR Band TOA Reflectance before and after optimal atmospheric model normalization.

Table 1: NIR Band TOA Reflectance Statistics Before and After Atmospheric Normalization.

Before Normalization			After Normalization		
Mean	STD	Uncertainty	Mean	STD	Uncertainty
0.40	0.0099	2.49%	0.40	0.0081	2.07%

SWIR1 Band:

Figure 5 shows the relationship between TOA reflectance and absolute humidity in the SWIR1 band. The regression slope was found to be statistically significant (p-value = approximately 3.28×10^{-4} at the 0.05 significance level), and indicated the negative relationship between TOA reflectance and absolute humidity. The model accounted for approximately 4.89% of the variability in the TOA reflectance.

As in the NIR band, the "optimal" atmospheric parameter model was found to be the initial linear model:

$$\rho_{model} = 0.4936 - 0.0005 \times AH \tag{13}$$

Figure 6 shows the resulting normalization provided with this model. As suggested by the low R^2 value, the normalization had little apparent effect on the overall data spread. This can also be observed in Table 2, where the temporal uncertainty shows only a slight reduction.
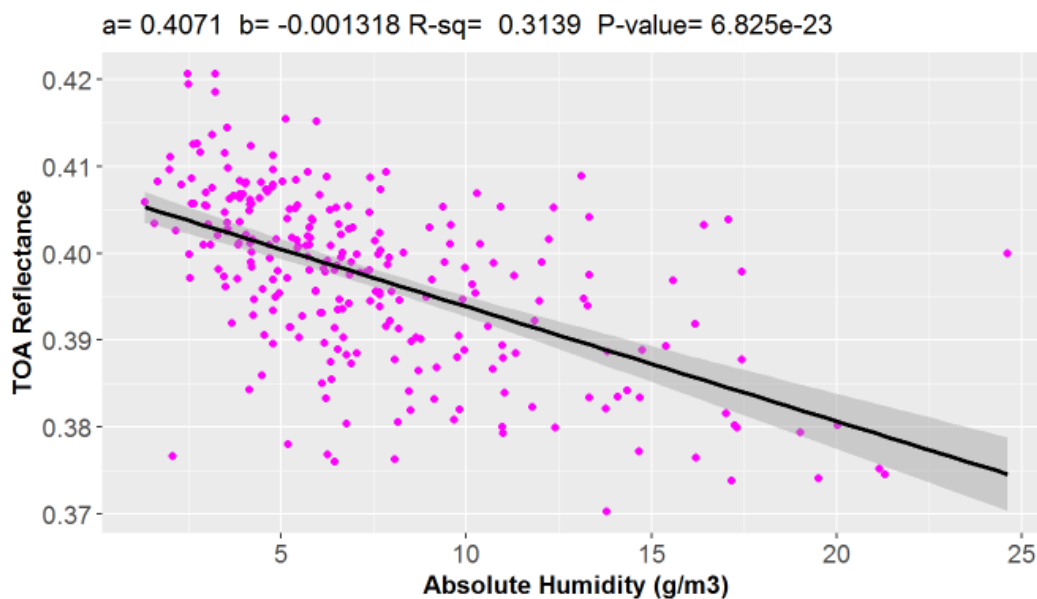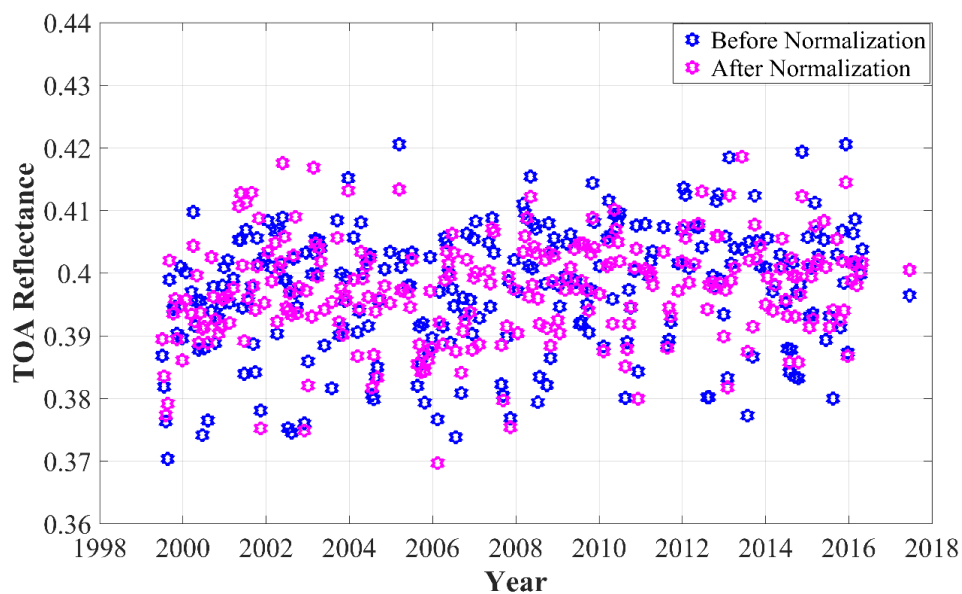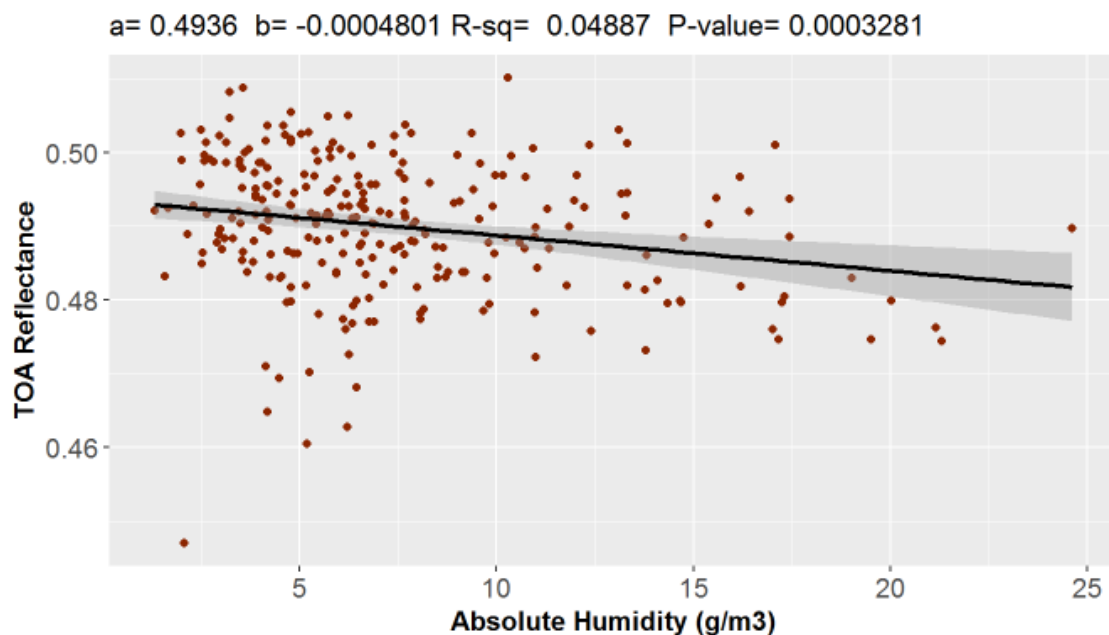

Figure 5: Linear Relationship between SWIR1 TOA Reflectance and Absolute Humidity.

Figure 6: SWIR1 Band TOA Reflectance before and after Optimal Atmospheric Model Normalization.

Table 2: SWIR1 Band TOA Reflectance Statistics Before and After Atmospheric Normalization.

Before Normalization			After Normalization		
Mean	STD	Uncertainty	Mean	STD	Uncertainty
0.49	0.0092	1.87 %	0.49	0.0089	1.82 %

SWIR2 Band:

Figure 7 shows the relationship between TOA reflectance and absolute humidity for the SWIR2 band. The slope of the regression line was found to be strongly statistically significant (p-value = approximately 4.35×10^{-12} at the 0.05 significance level) and indicated a negative relationship between TOA reflectance and absolute humidity. The model accounted for approximately 17% of the variability in the TOA reflectance.

Again, the initial linear model was identified as the "optimal" atmospheric model for this band:

$$\rho_{model} = 0.4422 - 0.0014 \times AH \tag{14}$$

Figure 8 shows the resulting normalization provided with this model. As in the NIR and SWIR1 bands, this normalization reduced the overall spread of the data, but increased the deviation from the mean for a few points, such as the early 2006 acquisition.

Table 3 shows the statistics before and after normalization. With the normalization, the temporal uncertainty has been reduced by approximately 0.32% in magnitude.

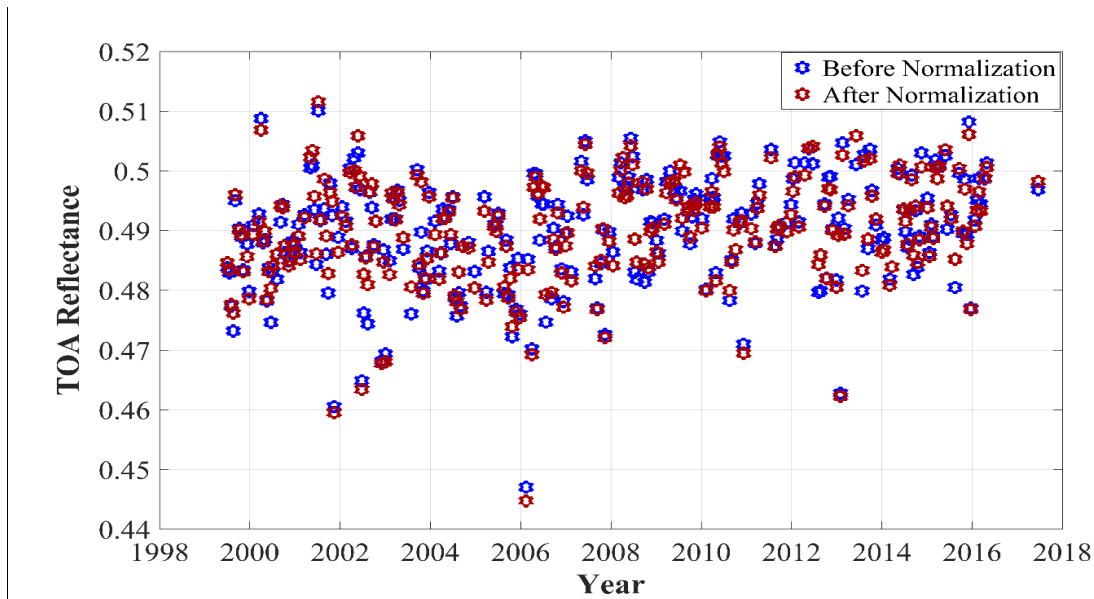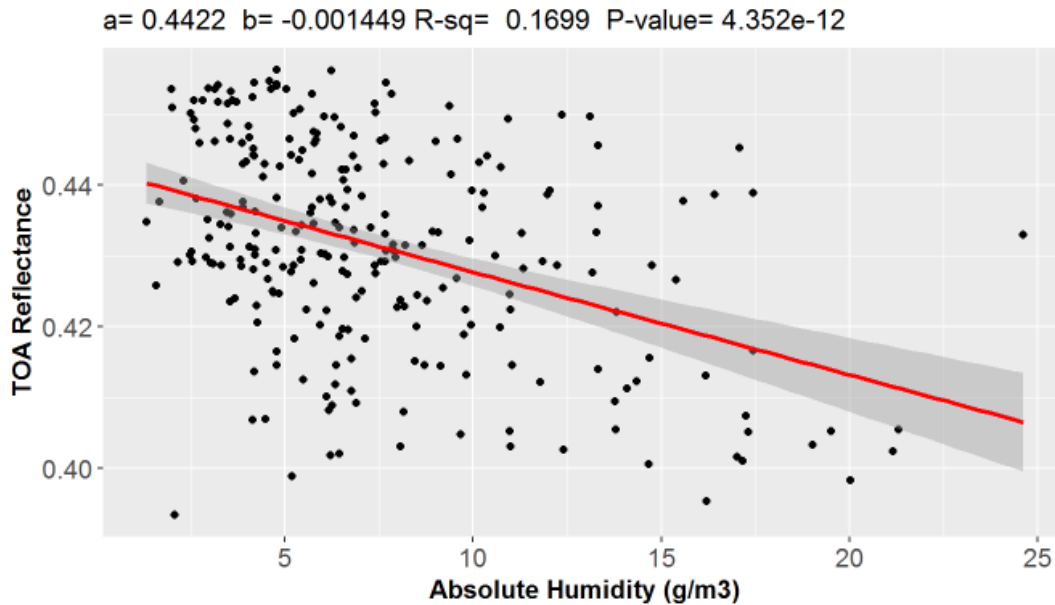Figure 7: Linear Relationship Between SWIR2 TOA Reflectance and Absolute Humidity.
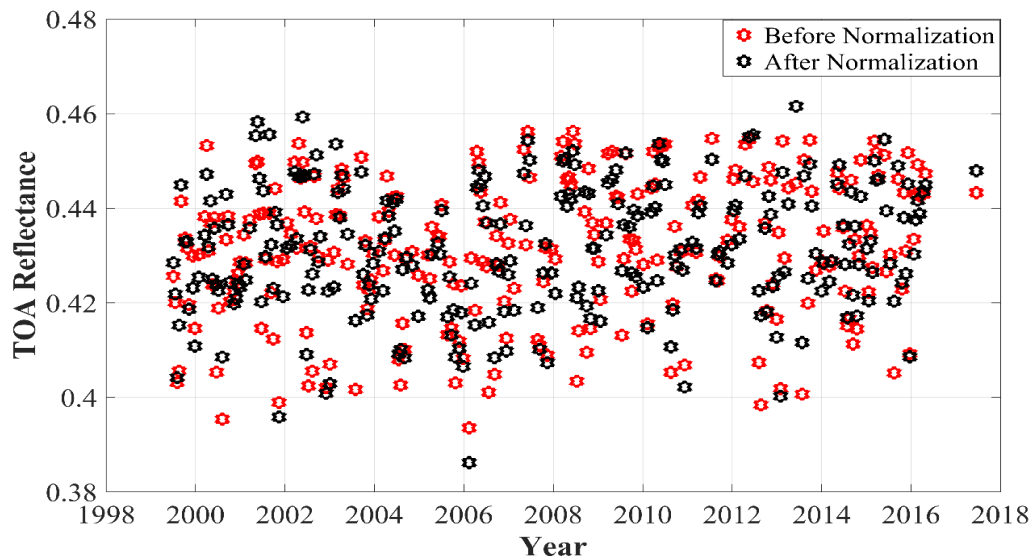

Figure 8: SWIR2 Band TOA Reflectance Before/After Optimal Atmospheric Model Normalization.

Table 3: SWIR2 Band TOA Reflectance Statistics Before and After Atmospheric Normalization

Before Normalization			After Normalization		
Mean	STD	Uncertainty	Mean	STD	Uncertainty
0.43	0.0148	3.43%	0.43	0.0134	3.11 %

3.1.2 Relationship Between TOA Reflectance and Atmospheric Pressure - Landsat 7 ETM+ Blue Band:

Figure 9 shows the relationship between TOA reflectance and atmospheric pressure in the Blue band. The regression slope was found to be statistically significant (p-value = approximately 4.95×10^{-4} at the 0.05 significance level), and indicated a positive relationship between TOA reflectance and atmospheric pressure. The model accounted for approximately 4.6% of the variability in TOA reflectance.

Based on the model R^2 values, the optimal atmospheric parameter model was found to consist of an exponential term and a constant term:

$$\rho_{model} = 0.2037 + 4.082 \times 10^{-16} \exp(p_{atm}) \tag{15}$$

The very small coefficient value on the exponential term ensures that for a range of realistic atmospheric pressures, the predicted reflectance will assume realistic values. The corresponding R^2 and p-values for the model were found to be approximately 0.04993 and 2.816×10^{-4}, respectively.

Figure 10 shows the resulting exponential model fit to the data. For the given pressure data, the two curves are very similar. The atmospheric model was able to slightly normalize the original TOA reflectance.

Figure 11 compares the reflectance trend before and after normalization. The apparent data spread changed little. The corresponding TOA reflectance statistics shown in Table 4 indicate little change in the overall temporal uncertainty, approximately 0.04% in magnitude.
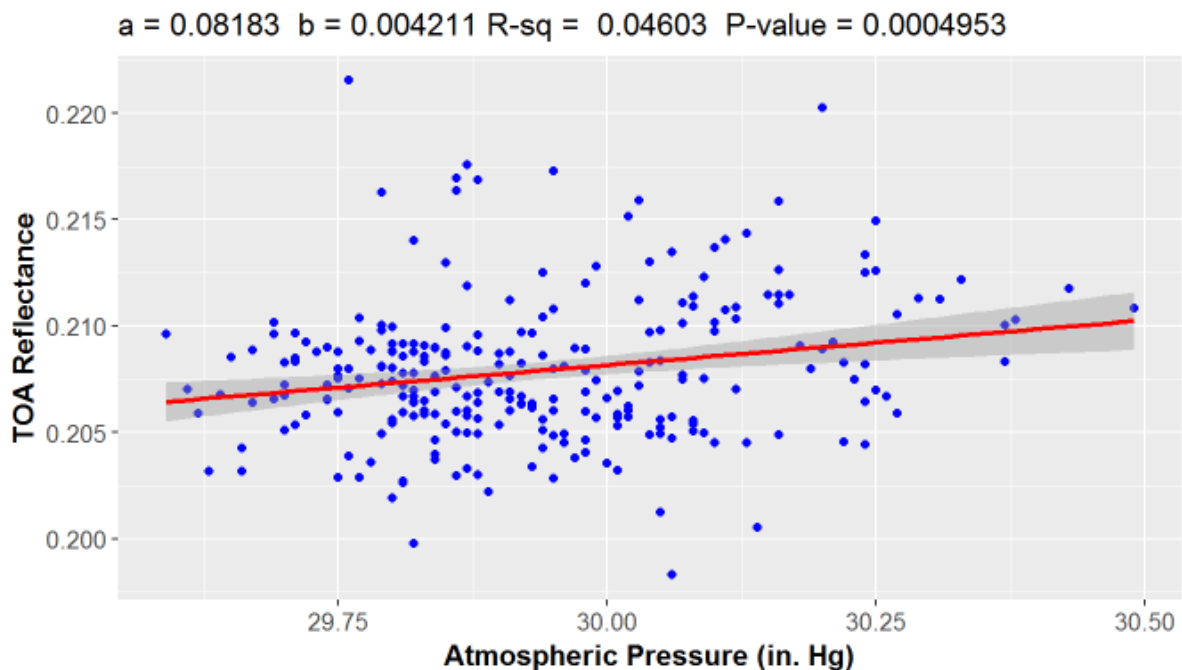
Figure 9: Linear relationship between Blue Band TOA Reflectance and Atmospheric Pressure.
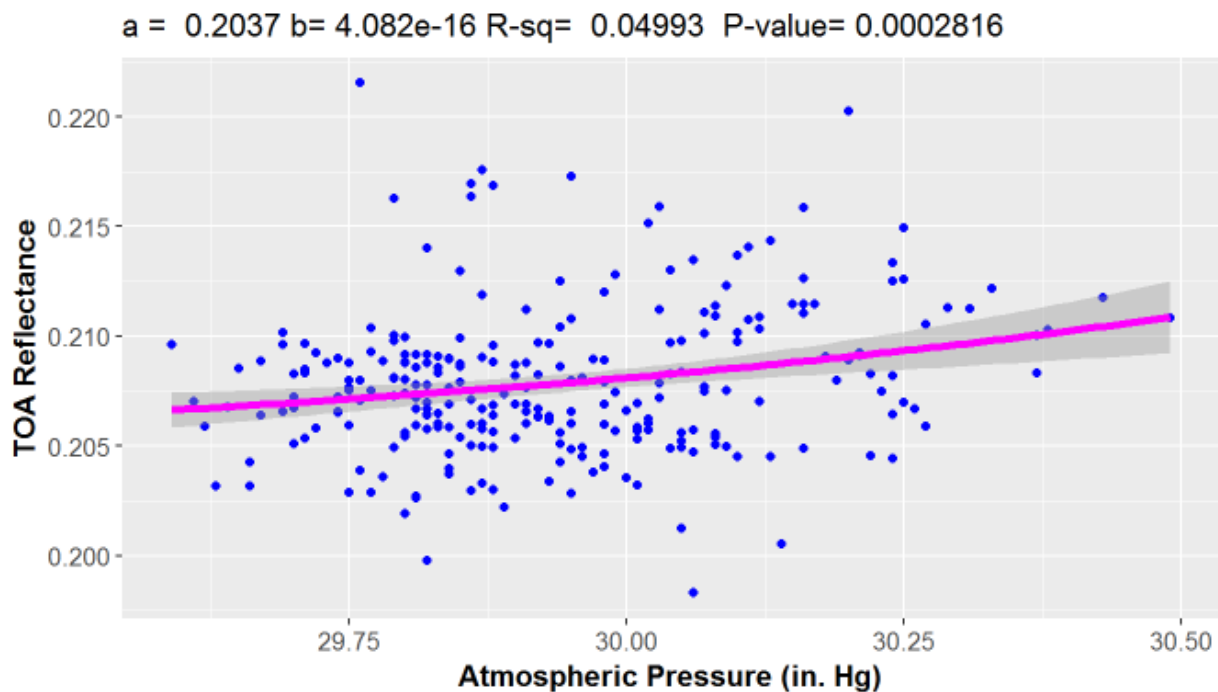
Figure 10: Exponential relationship between Blue Band TOA Reflectance and Atmospheric Pressure.

Figure 11: Blue Band TOA Reflectance Before/After Optimal Atmospheric Model Normalization.

Table 4: Blue Band TOA Reflectance Statistics Before and After Normalization with Optimal Atmospheric Model

Before Normalization			After Normalization		
Mean	STD	Uncertainty	Mean	STD	Uncertainty
0.21	0.0034	1.63%	0.21	0.0030	1.59 %

3.1.3   Relationship Between TOA Reflectance and Absolute Humidity—Landsat 8 OLI

SWIR2 Band:

For Landsat8 OLI only the SWIR2 band was shown to have a statistically significant relationship between TOA reflectance and absolute humidity. This is not surprising given that the OLI NIR and SWIR1 bands were narrowed in order to avoid significant water absorption features affecting the corresponding ETM+ bands (see Figure 1). In addition, the OLI SWIR2 RSR is quite similar in center wavelength location and bandwidth to the ETM+ SWIR2 RSR, as can be seen in Figure 1b; the analysis results should be consistent with those for the ETM+ SWIR2 band.

Figure 12 shows the expected negative relationship between TOA reflectance and absolute humidity for the SWIR2 band. The slope of the regression line was found to be statistically significant (*p*-value = approximately 3.4×10^{-6} at the 0.05 significance level). The model accounted for approximately 28% of the variability in the TOA reflectance, which was consistent with the R^2 value for the ETM+ linear model.

As with the ETM+ SWIR2 band, the "optimal" atmospheric parameter model was found to be the initial linear model. Given the similarity in spectral responses, the model coefficients were consistent with the corresponding ETM+ model coefficients.

$$\rho_{model} = 0.4759 - 0.0020 \times AH \tag{16}$$

Figure 13 shows the resulting normalization provided with this model. As with the ETM+ SWIR2 band, the normalization visibly reduced the overall data spread. Interestingly, no reflectance appeared to be significantly over-normalized.

Table 5 shows the statistics before and after the normalization. The temporal uncertainty was reduced approximately 0.45% in magnitude.

Figure 12: Linear Relationship between SWIR2 Band TOA Reflectance and Absolute Humidity.
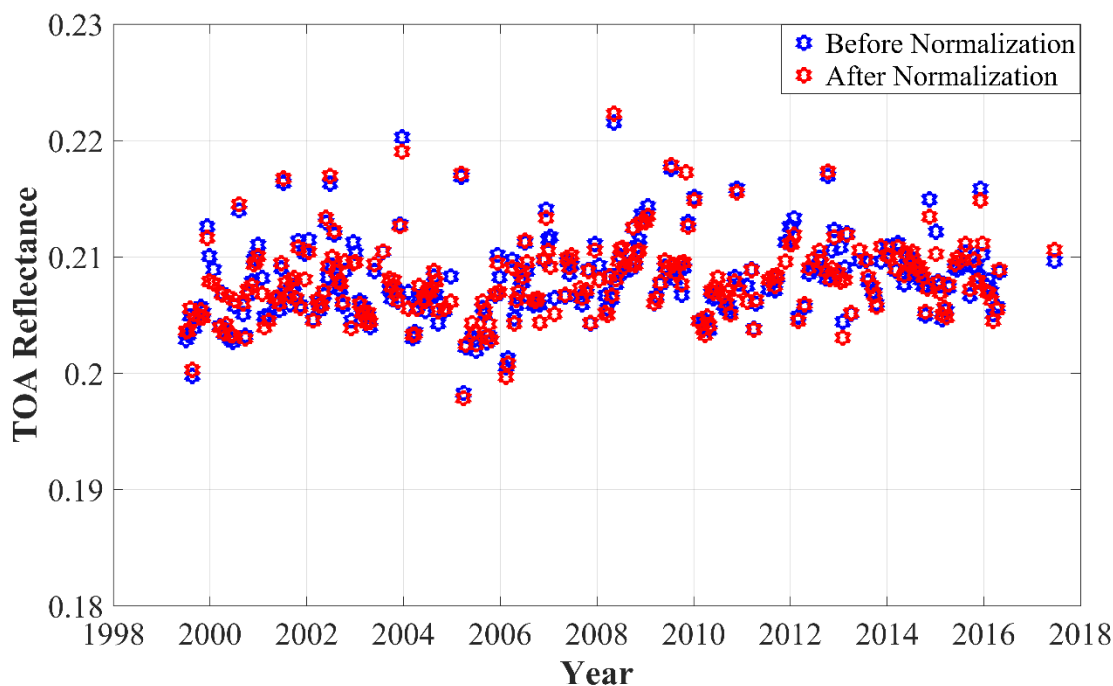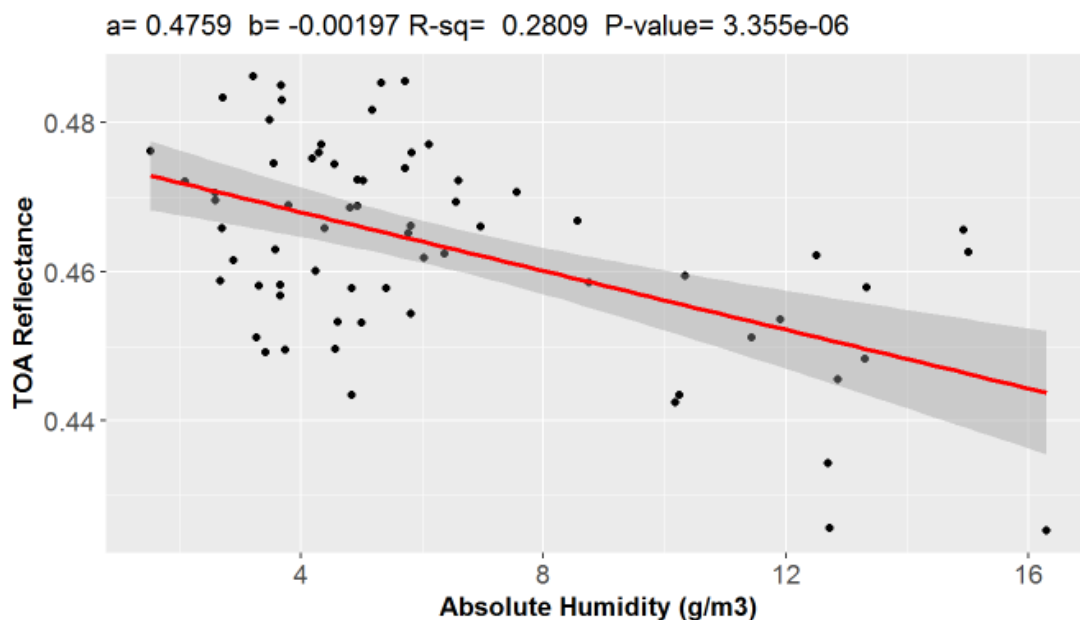
Figure 13: SWIR2 Band TOA Reflectance Before/After Optimal Atmospheric Model Normalization.

Table 5: SWIR2 Band TOA Reflectance Statistics Before and After Atmospheric Normalization

Before Normalization			After Normalization		
Mean	STD	Uncertainty	Mean	STD	Uncertainty
0.46	0.0136	2.93%	0.46	0.0116	2.48 %

3.1.4 Relationship Between TOA Reflectance and Atmospheric Pressure--Landsat8 OLI

As with the ETM+, the Blue band was shown to have a statistically significant relationship between TOA reflectance and atmospheric pressure. Not surprisingly, the Coastal/Aerosol band was also shown to have a statistically significant relationship, as was the Green band. The resulting optimal models were found to be exponential in nature. However, the exponential plots were visually almost indistinguishable from the linear plots, as can be seen in Figures 9 and 10. Consequently, plots of the exponential model fits will not be shown here.

Coastal/Aerosol Band:

Figure 14 shows the relationship between TOA reflectance and atmospheric pressure in the Coastal/Aerosol band. The regression slope was found to be statistically significant (p-value =

approximately 4.97×10^{-5} at the 0.05 significance level), and indicated a positive relationship between TOA reflectance and atmospheric pressure. The model accounted for approximately 22.2% of the variability in TOA reflectance.

Based on the model R^2 values, the optimal atmospheric parameter model was found to consist of an exponential term and a constant term. The R^2 and p-value for this model were found to be approximately 0.02239 and 4.6×10^{-5} respectively.

$$\rho_{model} = 0.1982 + 1.002 \times 10^{-15} \exp(p_{atm}) \tag{17}$$

Figure 15 shows the trend comparison before and after normalization. It can be seen that the atmospheric model was able to normalize the original TOA reflectance significantly. However, some of the lower reflectance data points, such as the two acquisitions in early 2017, were reduced further away from the overall reflectance mean.

Table 6 shows the statistics before and after normalization using atmospheric model. It can be noticed that the temporal uncertainty was reduced by approximately 0.22% in magnitude.

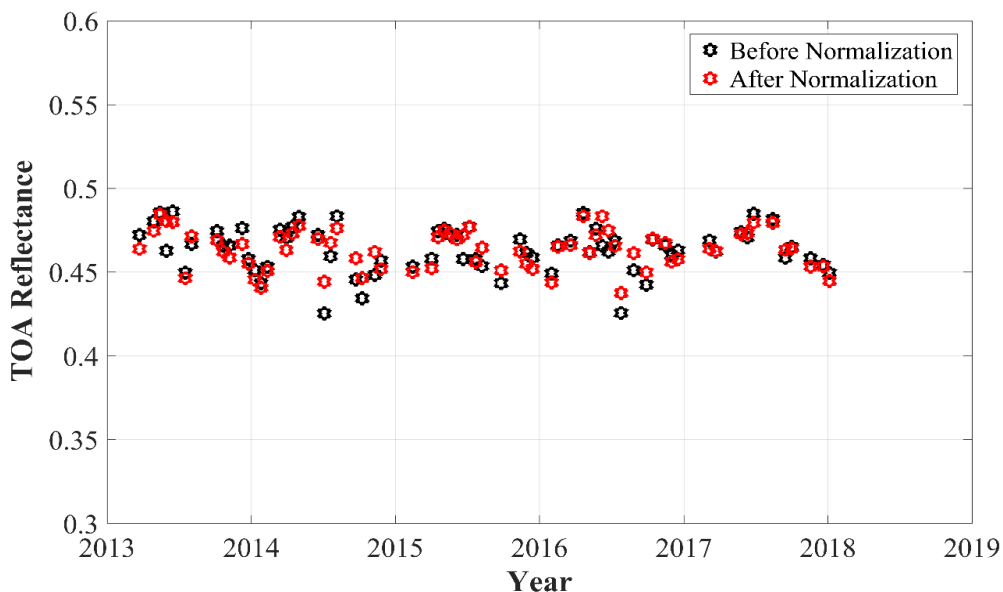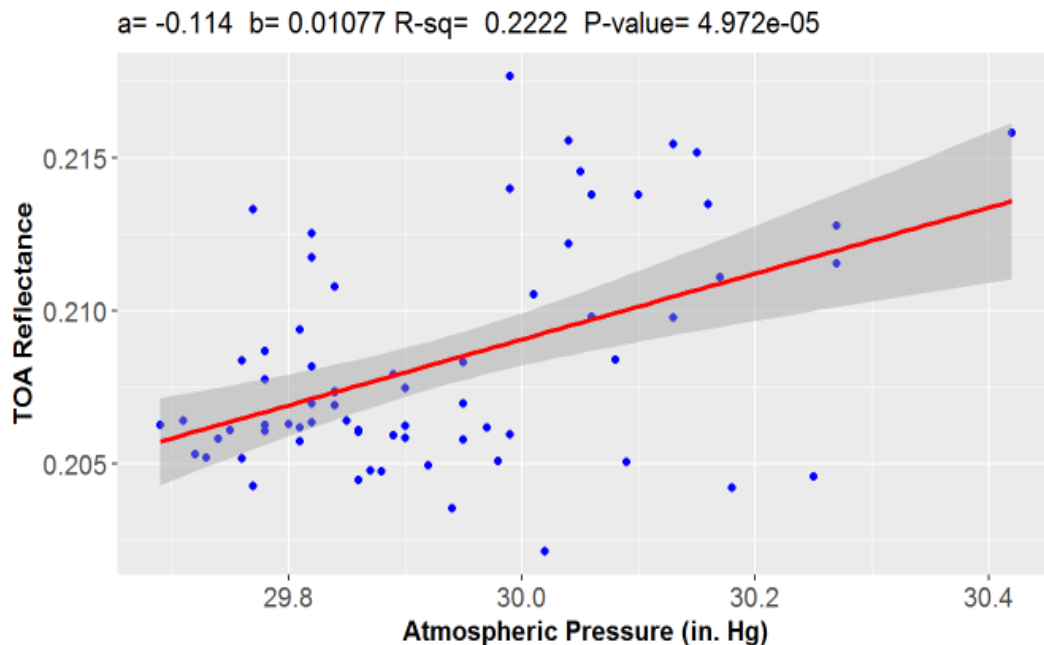Figure 14: Linear Relationship between C/A Band TOA Reflectance and Atmospheric Pressure.

Figure 15: C/A Band TOA Reflectance Before/After Optimal Atmospheric Model Normalization.

Table 6: CA Band TOA Reflectance Statistics Before and After Optimal Atmospheric Model Normalization

Before Normalization			After Normalization		
Mean	STD	Uncertainty	Mean	STD	Uncertainty
0.21	0.0036	1.75%	0.21	0.0032	1.53 %

Blue Band:

Figure 16 shows the relationship between TOA reflectance and atmospheric pressure in the Blue band. The regression slope was found to be somewhat statistically significant (*p*-value = approximately 0.015 at the 0.05 significance level), and indicated a positive relationship between TOA reflectance and atmospheric pressure. The model accounted for approximately 8.7% of the variability in the TOA reflectance.

Similar to the Coastal/Aerosol band, based on the model R^2 values, the optimal atmospheric parameter model was found to consist of an exponential function and a constant term. The R^2 and p-value for this model were found to be approximately 0.0916 and 0.0121, respectively.

$$\rho_{model} = 0.2084 + 4.988 \times 10^{-16} \exp(p_{atm}) \tag{18}$$

Figure 17 shows the trend comparison before and after normalization. Not surprisingly, the overall uncertainty (Table 7) was reduced by approximately 0.07% in magnitude, a slight change.

Figure 16: Linear Relationship Between Blue Band TOA Reflectance and Atmospheric Pressure.
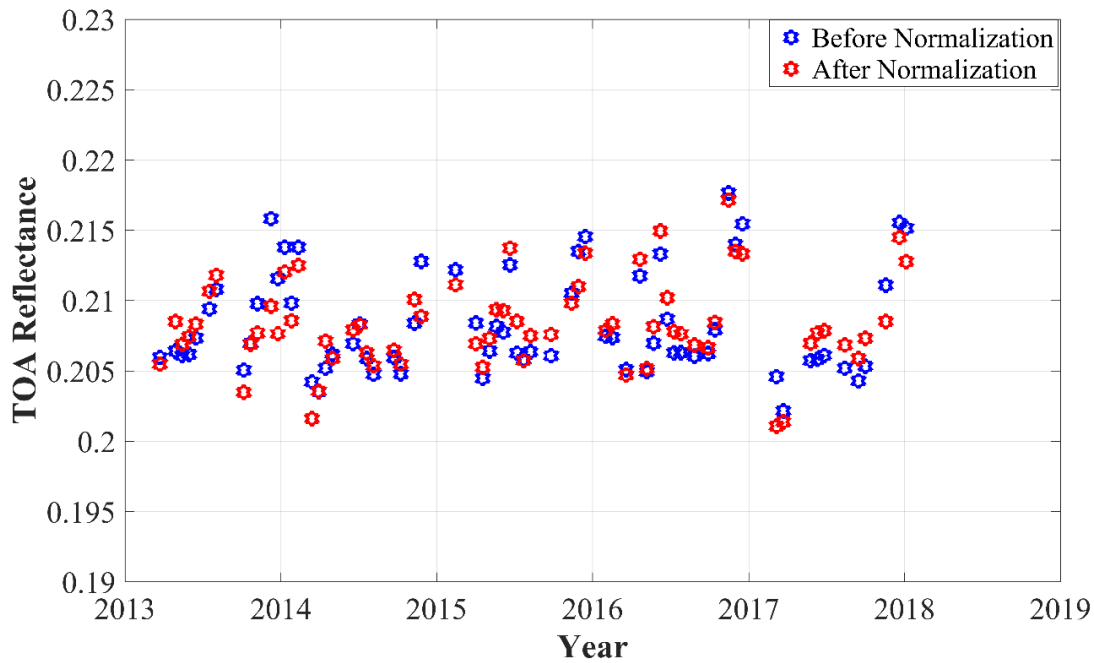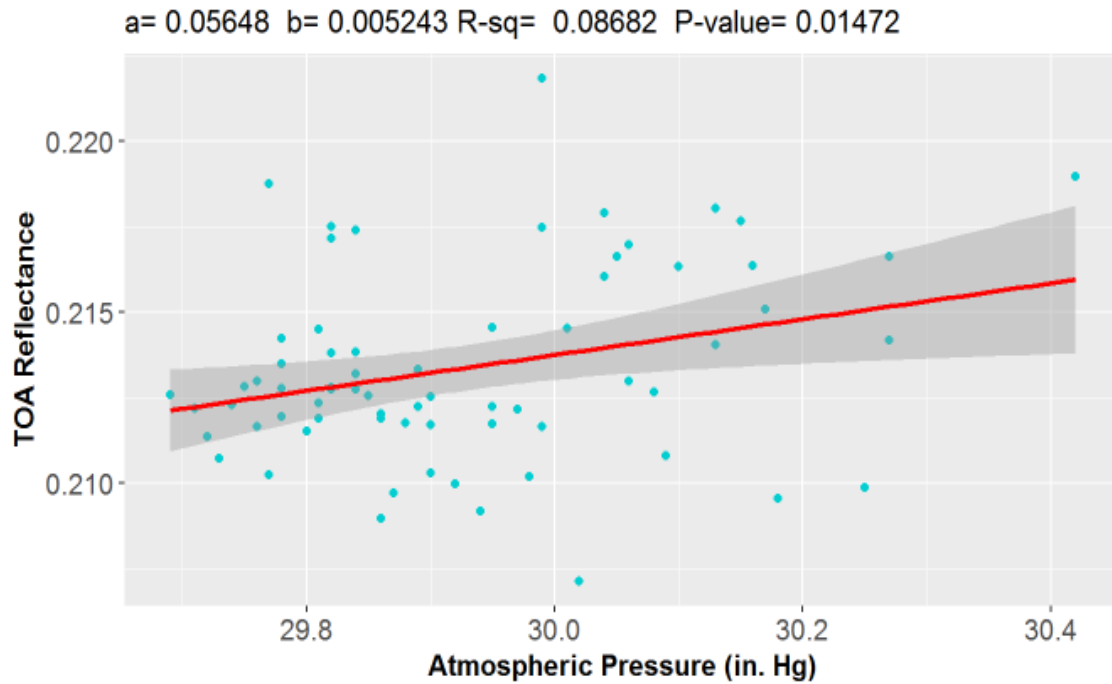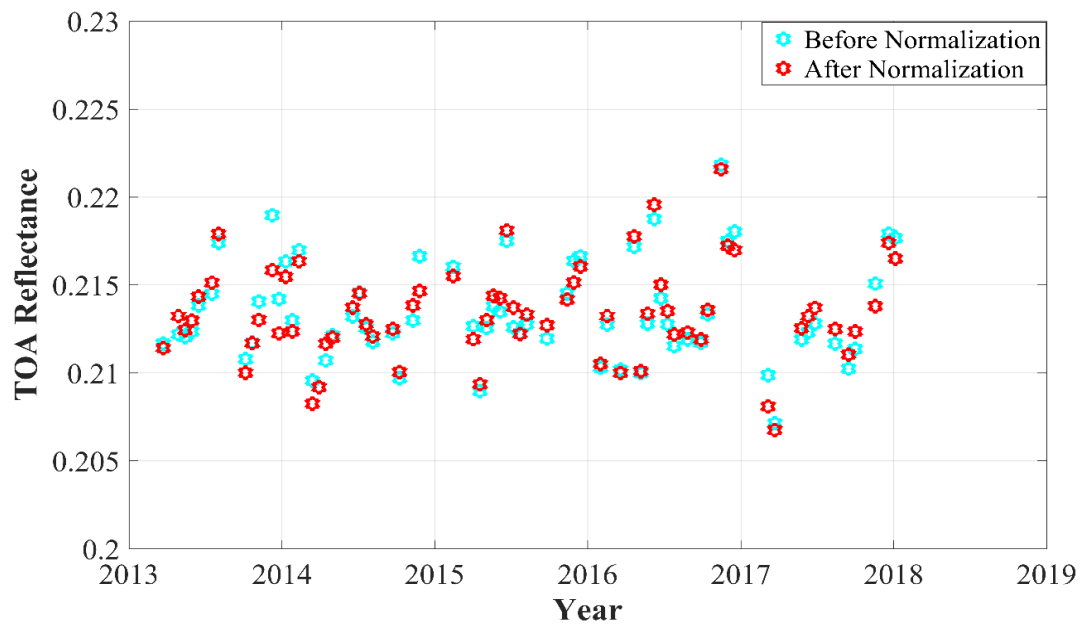

Figure 17: Blue Band TOA Reflectance Before/After Optimal Atmospheric Model Normalization.

Table 7: Blue Band TOA Reflectance Statistics Before and After Optimal Atmospheric Model Normalization

Before Normalization			After Normalization		
Mean	STD	Uncertainty	Mean	STD	Uncertainty
0.21	0.0028	1.33%	0.21	0.0027	1.26 %

Green Band:

Figure 18 shows the relationship between TOA reflectance and atmospheric pressure in the Green band. The regression slope was found to be marginally statistically significant (p-value = approximately 0.033 at the 0.05 significance level), and indicated a negative relationship between TOA reflectance and atmospheric pressure. The model accounted for approximately 6.7% of the variability in TOA reflectance.

The "optimal" atmospheric model consisted of a constant term and an exponential term. The R^2 and p-value for this model were found to be approximately 0.0723 and 0.031, respectively--slightly better than the linear model.

$$\rho_{model} = 0.2689 - 4.327 \times 10^{-16}\exp(p_{atm}) \tag{19}$$

Figure 19 shows the trend comparison before and after normalization. The atmospheric model was able to slightly normalize the original TOA reflectance.

Table 8 shows the statistics before and after normalization using atmospheric model. It can be noticed that the overall uncertainty was reduced by approximately 0.04% in magnitude, a slight change.

a= 0.4158 b= -0.005053 R-sq= 0.06698 P-value= 0.03309
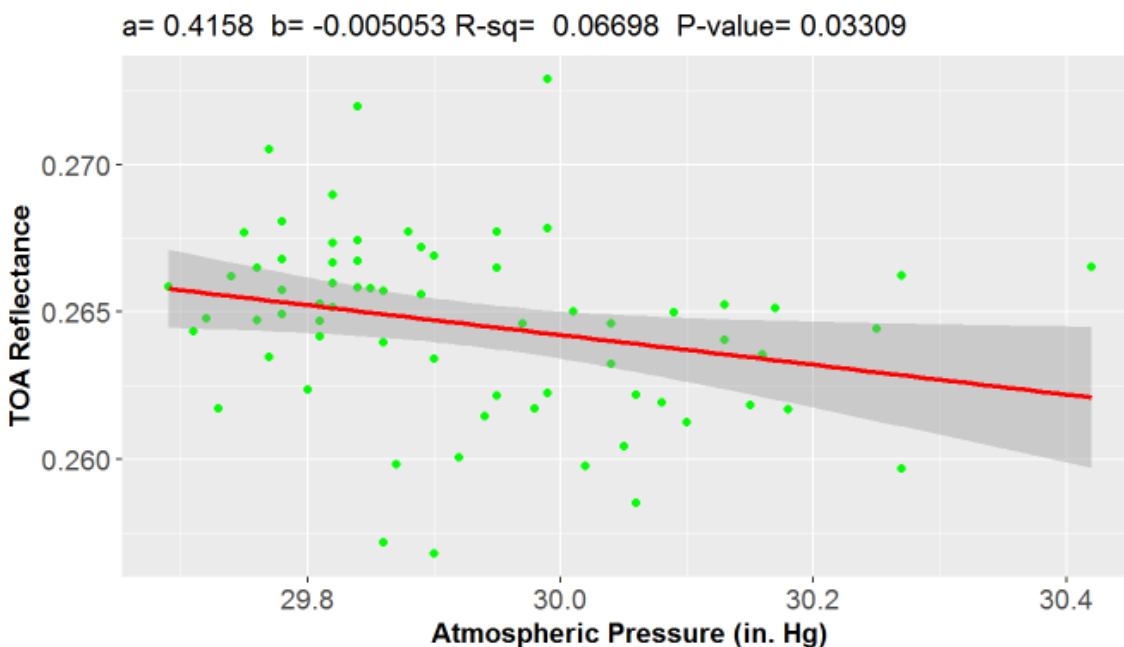
Figure 18: Linear Relationship between Green Band TOA Reflectance and Atmospheric Pressure.
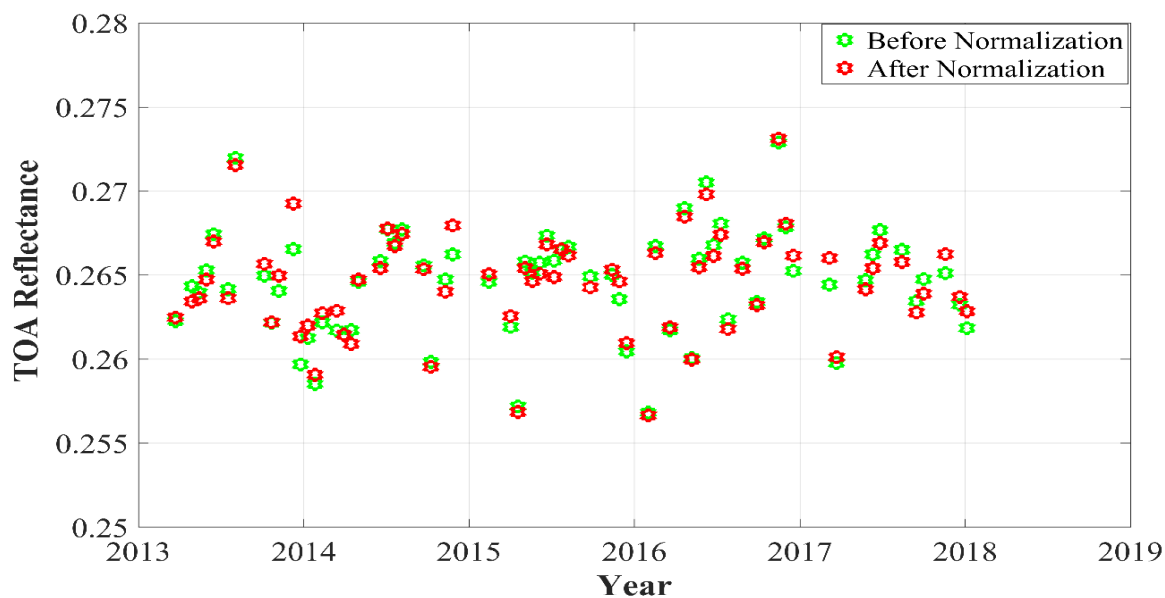
Figure 19: Green Band TOA Reflectance Before/After Optimal Atmospheric Model Normalization.

Table 8: Green Band TOA Reflectance Statistics Before and After Optimal Atmospheric Model Normalization

Before Normalization			After Normalization		
Mean	STD	Uncertainty	Mean	STD	Uncertainty
0.26	0.0031	1.18%	0.26	0.0030	1.14

3.2 Wadi ad-Dawasir Desert Site

This section presents the characterization results obtained for the Wadi ad-Dawasir site. Only the results for the OLI are presented, as there was insufficient weather station data available to allow a similar analysis for the ETM+.

3.2.1 Relationship Between TOA Reflectance and Absolute Humidity

Figure 20 shows the relationship between TOA reflectance and absolute humidity for the SWIR2 band. The slope of the regression line was found to be statistically significant (*p*-value = approximately $3.27x10^{-3}$ at the 0.05 significance level) and indicated a negative relationship between TOA reflectance and absolute humidity. The model accounted for approximately 10.7% of the variability in the TOA reflectance.

As in the SWIR2 band, the "optimal" atmospheric parameter model was found to be the initial linear model:

$$\rho_{model} = 0.4696 - 0.0014 \times AH \tag{20}$$

Figure 21 shows the resulting normalization provided with this model. The normalization visibly reduced the overall spread of the data. Reflectances for some of the data points, such as the early 2017 acquisition, appeared to be over normalized.

Table 9 shows the statistics before and after normalization using atmospheric model. The overall uncertainty was reduced by approximately 0.16% in magnitude.

a= 0.4696 b= -0.001411 R-sq= 0.1069 P-value= 0.00327
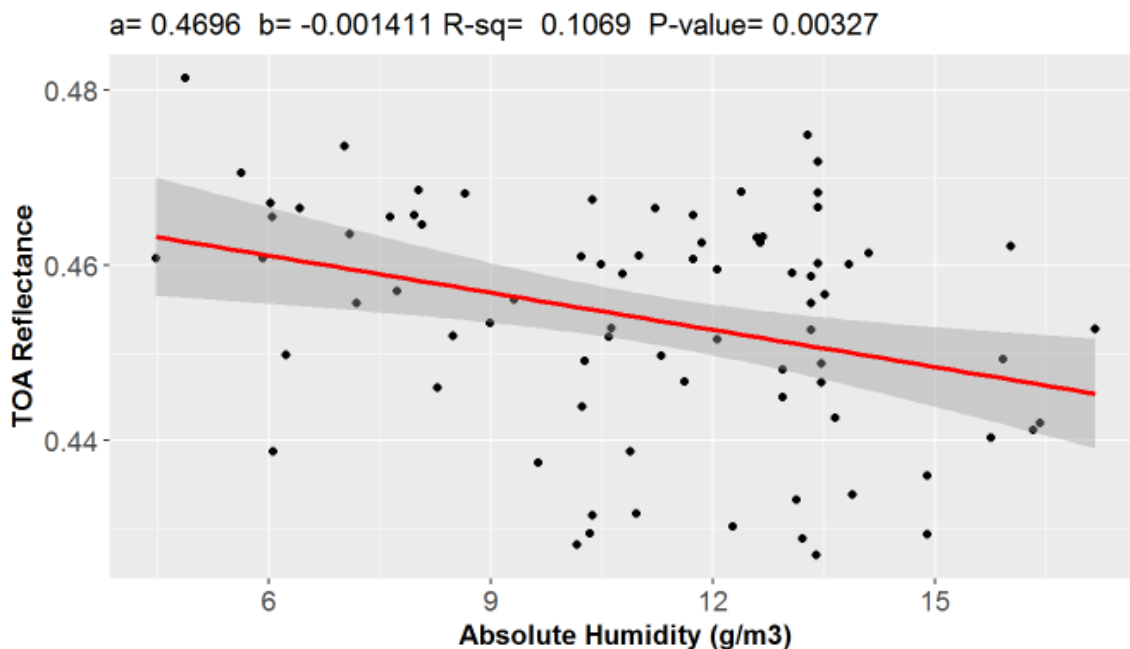
Figure 20: Linear Relationship Between SWIR2 Band TOA Reflectance and Absolute Humidity.

Figure 21: SWIR2 Band TOA Reflectance Before/After Optimal Atmospheric Model Normalization.

Table 9: SWIR2 Band TOA Reflectance Statistics Before and After Atmospheric Normalization

Before Normalization			After Normalization		
Mean	STD	Uncertainty	Mean	STD	Uncertainty
0.45	0.0130	2.88%	0.46	0.0116	2.72 %

3.2.2 Relationship Between TOA Reflectance and Atmospheric Pressure

Coastal/Aerosol Band:

Figure 22 shows the relationship between TOA reflectance and atmospheric pressure in the Coastal/Aerosol band. The regression slope was found to be marginally statistically significant (*p*-value = approximately 0.043 at the 0.05 significance level), and, interestingly, indicated a negative relationship between TOA reflectance and atmospheric pressure. The model accounted for approximately 5.2% of the variability in the TOA reflectance.

The "optimal" atmospheric parameter model for this band consisted of an exponential term and a constant term. The R^2 and p-value for this model were found to be 0.0537 and 0.0391 respectively.

$$\rho_{model} = 0.2151 - 7.283 \times 10^{-16}\exp(p_{atm}) \tag{21}$$

Figure 23 shows the trend comparison before and after normalization. The observed data spread was slightly reduced. However, no data points appeared to be significantly over-normalized. The corresponding uncertainty, as shown in Table 10, was reduced by approximately 0.06% in magnitude.

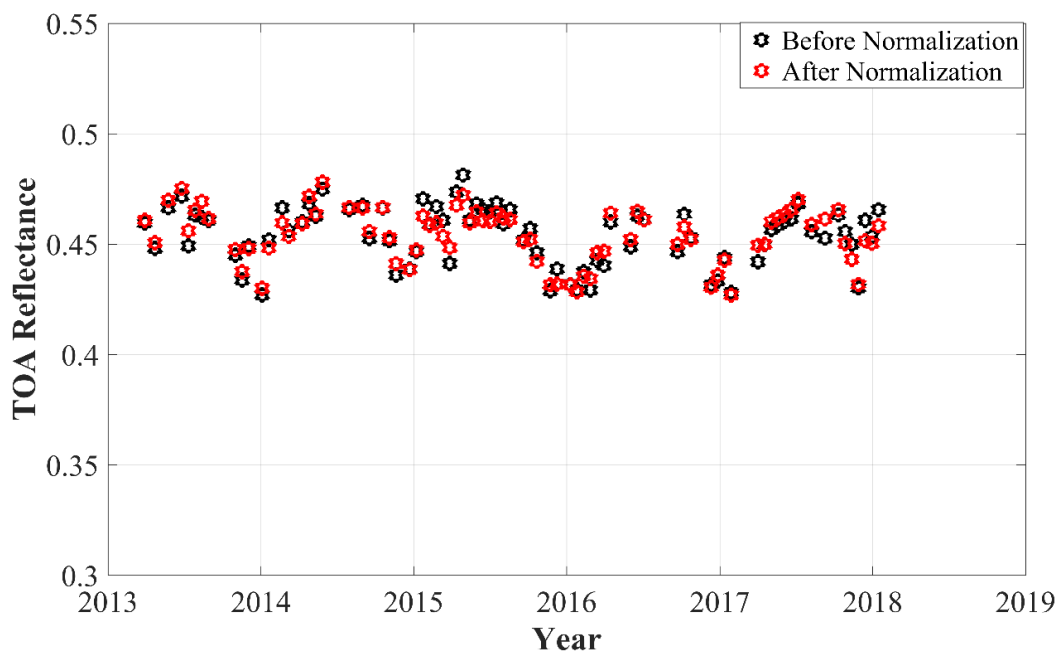

Figure 22: Linear Relationship Between C/A TOA Reflectance and Atmospheric Pressure.

Figure 23: C/A Band TOA Reflectance Before/After Optimal Atmospheric Model Normalization.

Table 10: Coastal/Aerosol Band TOA Reflectance Statistics Before and After Optimal
Atmospheric Model Normalization.

Before Normalization			After Normalization		
Mean	STD	Uncertainty	Mean	STD	Uncertainty
0.21	0.0060	2.88%	0.21	0.0058	2.82 %

Blue Band:

Figure 24 shows the relationship between TOA reflectance and atmospheric pressure in the Blue band. The regression slope was found to be statistically significant (p-value = approximately 4.25×10^{-3} at the 0.05 significance level), and indicated a negative relationship between TOA reflectance and atmospheric pressure. The model accounted for approximately 10.1% of the variability in TOA reflectance.

The "optimal" atmospheric model consisted of an exponential term and a constant term. The R^2 and p-value for this model were found to be 0.1014 and 0.0042, respectively.

$$\rho_{model} = 0.2210 - 1.113 \times 10^{-15} \exp(p_{atm}) \tag{22}$$

Figure 25 shows the trend comparison before and after normalization. The overall spread of the data was reduced with the normalization. The reflectance from the early 2015 acquisition appeared to be over normalized.

Table 10 shows the statistics before and after normalization using atmospheric model. It can be noticed that the overall uncertainty was reduced by approximately 0.16% in magnitude.

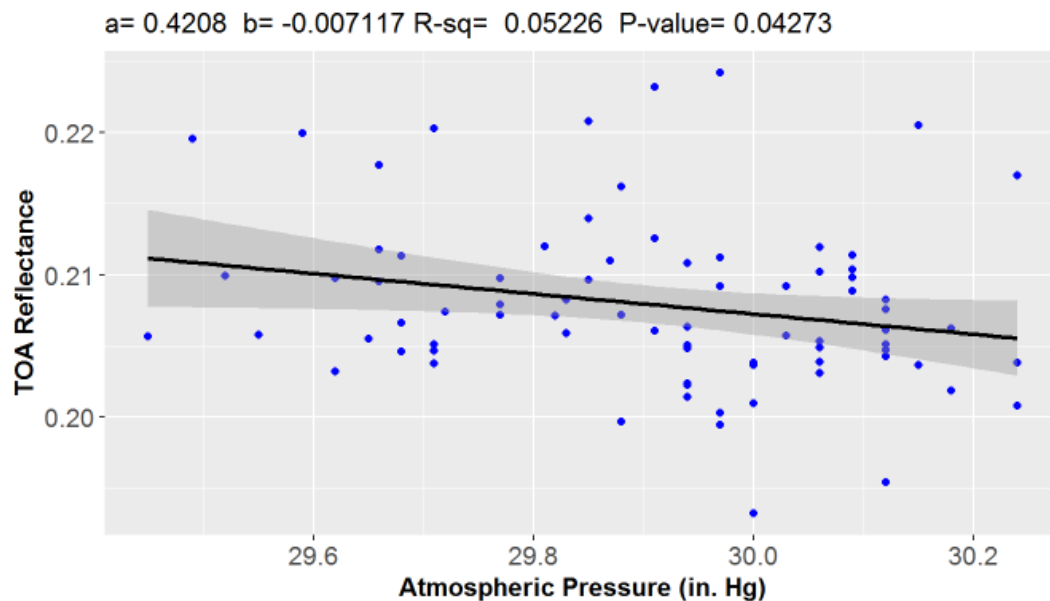a= 0.5294 b= -0.01068 R-sq= 0.1013 P-value= 0.004251

Figure 24: Linear Relationship Between Blue Band TOA Reflectance and Atmospheric Pressure.
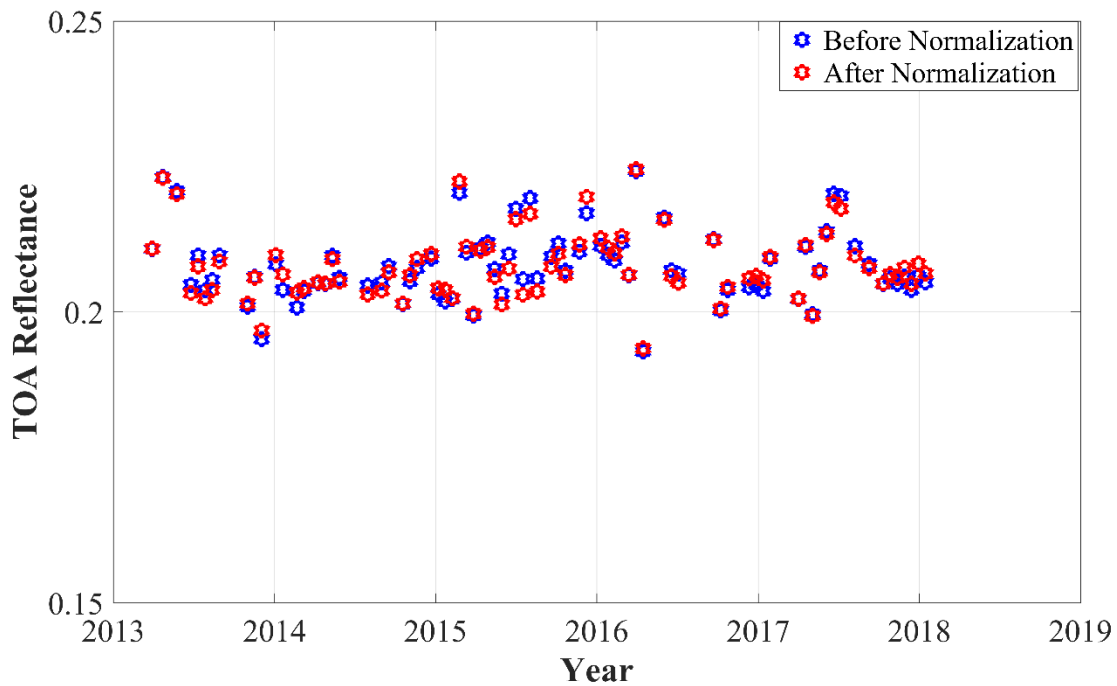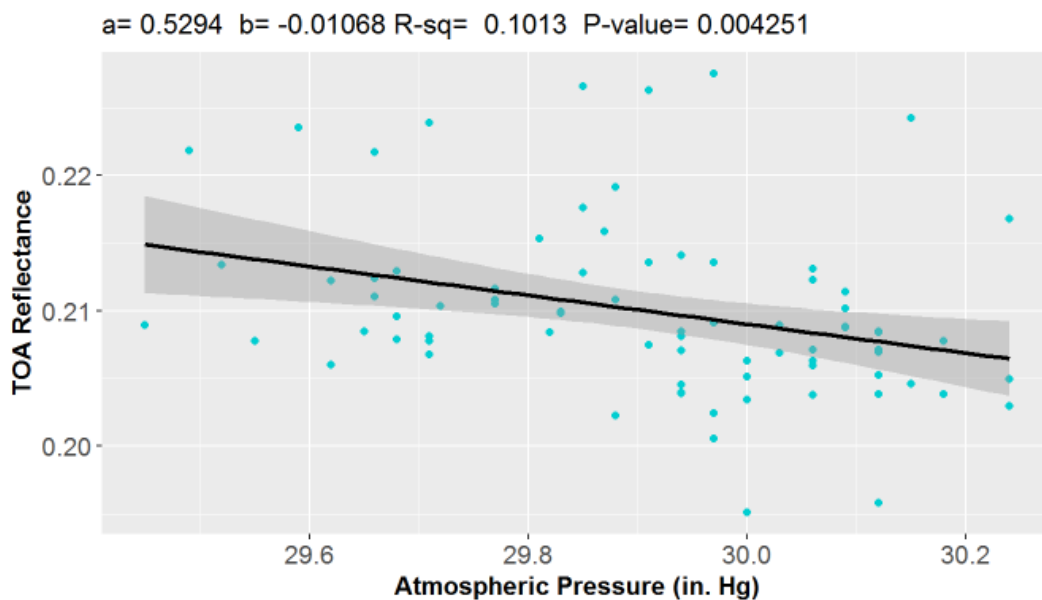

Figure 25: Blue Band TOA Reflectance Before/After Optimal Atmospheric Model Normalization.

Table 11: Blue Band TOA Reflectance Statistics Before and After Optimal Atmospheric Model Normalization.

Before Normalization			After Normalization		
Mean	STD	Uncertainty	Mean	STD	Uncertainty
0.21	0.0064	3.08%	0.21	0.0061	2.92 %

Green Band:

Figure 26 shows the relationship between TOA reflectance and atmospheric pressure in the Green band. The regression slope was found to be statistically significant (p-value = approximately 2.55×10^{-3} at the 0.05 significance level), and indicated a negative relationship between TOA reflectance and atmospheric pressure. The model accounted for approximately 11.2% of the variability in TOA reflectance.

The "optimal" atmospheric model consisted of an exponential term and a constant term. The R^2 and p-value for this model were found to be 0.1169 and 0.0020 respectively.

$$\rho_{model} = 0.2617 - 1.110 \times 10^{-15} \exp(p_{atm}) \tag{23}$$

Figure 27 shows the trend comparison before and after normalization. Again, the overall data spread was reduced with the normalization. The reflectance data from the acquisition in early 2015 appeared to be over-normalized in this band as well. The corresponding overall temporal uncertainty was reduced by approximately 0.15% in magnitude, as shown in Table 12.

a= 0.5624 b= -0.01042 R-sq= 0.1122 P-value= 0.002551
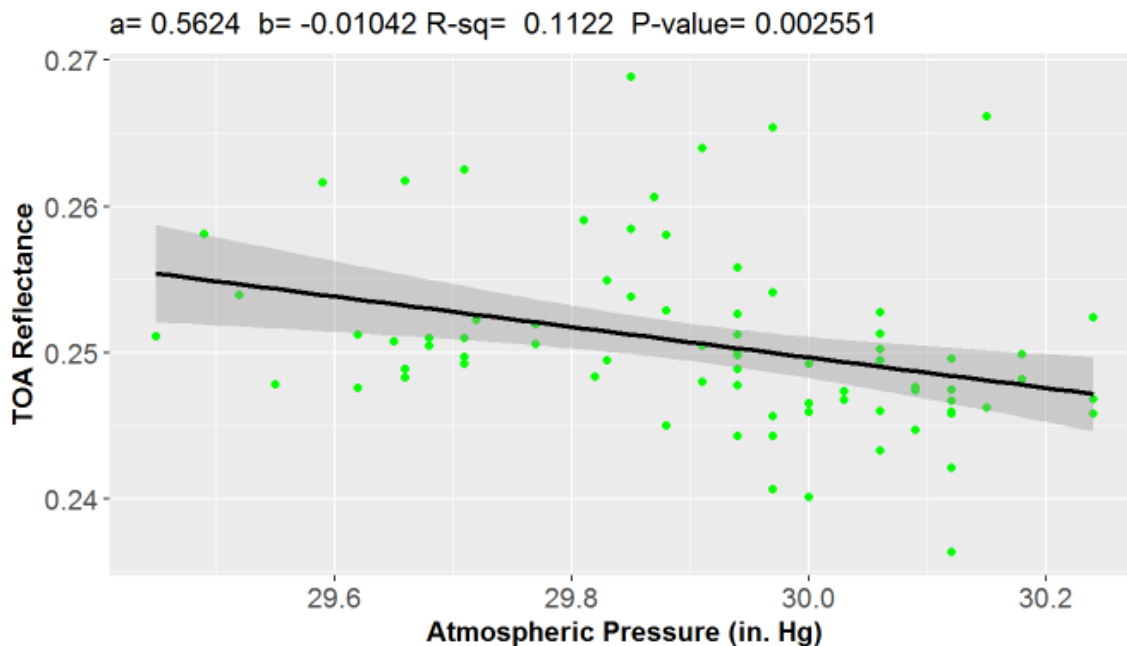
Figure 26: Linear Relationship between Green Band TOA Reflectance and Atmospheric Pressure.
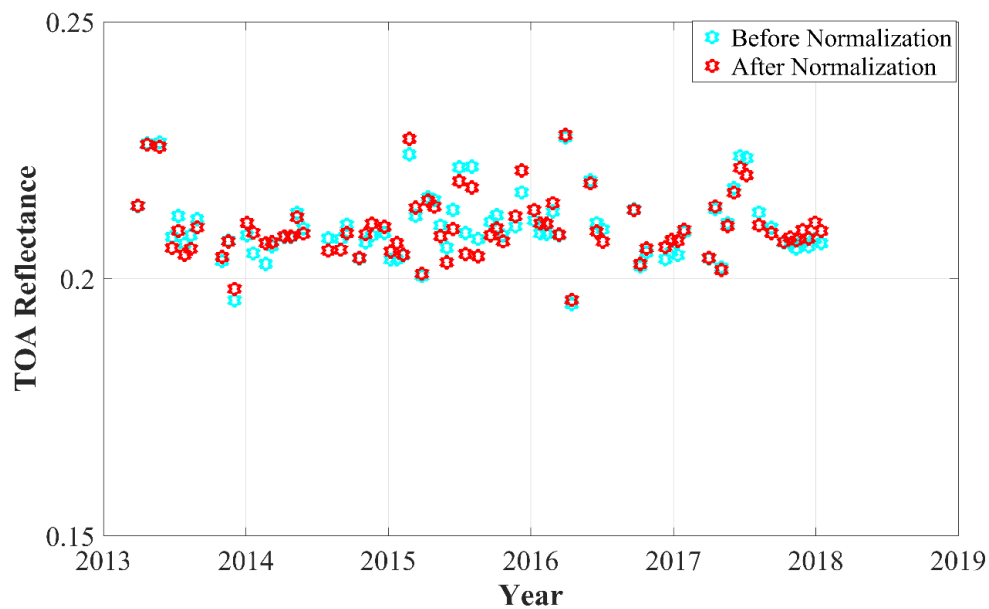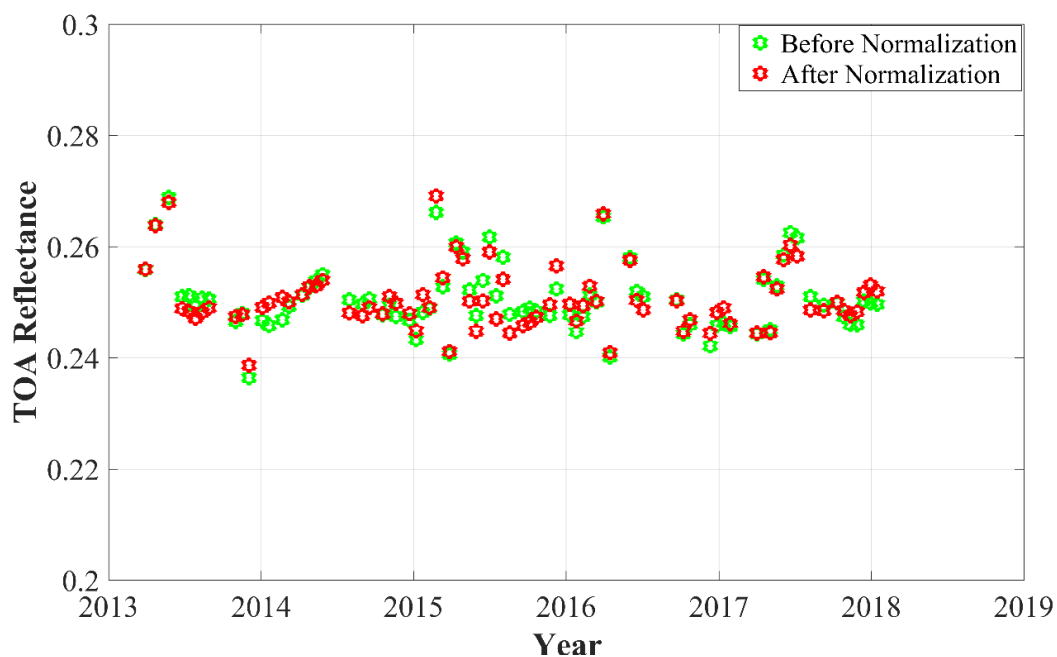

Figure 27: Green Band TOA Reflectance Before/After Optimal Atmospheric Model Normalization.

Table 12: Green Band TOA Reflectance Statistics Before and After Optimal Atmospheric Model Normalization

Before Normalization			After Normalization		
Mean	STD	Uncertainty	Mean	STD	Uncertainty
0.25	0.0060	2.40%	0.25	0.0056	2.25

3.3 Effects of BRDF Normalization

The spread in TOA reflectance data was reduced to varying degrees with atmospheric normalization. The amount of reduction varied by band, with more reduction apparent at longer wavelengths. At this stage, BRDF normalization was not performed. One question to be answered was whether BRDF normalization would effectively reduce the reflectance variability even further, especially at shorter wavelengths.

As mentioned in Chapter 2, once the TOA reflectance data were normalized with the optimal atmospheric parameter models, BRDF normalization was performed using a two-angle quadratic model for Algodones Dunes and a four-angle linear model for Wadi-ad-Dawasir. For the purposes of this analysis, this normalization order was chosen in order to "preserve" the statistical significance of the relationship between the atmospheric parameter of interest and TOA reflectance. If BRDF normalization was performed before attempting atmospheric modeling in the shorter wavelength bands, the statistical significance of the relationship was significantly weakened or eliminated entirely. Following BRDF normalization, the overall uncertainty at both sites was determined for both sensors. The summarized results are shown in Tables 13 and 14 for Algodones Dunes, and Table 15 for Wadi-ad-Dawasir.

Algodones Dunes:

For both sensors, the SWIR bands are more sensitive to BRDF effects. The OLI NIR band is less sensitive to BRDF than the ETM+ -- not surprising given the significant narrowing and center location shift in the OLI band.

Table 13: TOA Reflectance Summary Statistics for ETM+ Bands After Atmospheric and BRDF Normalization.

Bands	Before Atmospheric Normalization			After Atmospheric Normalization			Uncertainty After BRDF Normalization (%)
	Mean	STD	Uncertainty (%)	Mean	STD	Uncertainty (%)	
Blue	0.21	0.0034	1.63	0.21	0.0030	1.59	1.44
Green	0.26	0.0039	1.48	0.26	0.0039	1.48	1.36
Red	0.35	0.0056	1.59	0.35	0.0056	1.59	1.41
NIR	0.40	0.0099	2.49	0.40	0.0081	2.07	2.01
SWIR1	0.49	0.0092	1.87	0.49	0.0089	1.82	1.66
SWIR2	0.43	0.0148	3.43	0.43	0.0134	3.11	2.69

Table 14: TOA Reflectance Summary Statistics for OLI Bands After Atmospheric and BRDF Normalization.

Bands	Before Atmospheric Normalization			After Atmospheric Normalization			Uncertainty After BRDF Normalization (%)
	Mean	STD	Uncertainty (%)	Mean	STD	Uncertainty (%)	
CA	0.21	0.0036	1.75	0.21	0.0032	1.53	1.14
Blue	0.21	0.0028	1.33	0.21	0.0027	1.26	0.97
Green	0.26	0.0031	1.18	0.26	0.0030	1.14	0.95
Red	0.35	0.0044	1.26	0.35	0.0044	1.26	1.00
NIR	0.43	0.0046	1.05	0.43	0.0046	1.05	0.92
SWIR1	0.50	0.0074	1.48	0.50	0.0074	1.48	0.90
SWIR2	0.46	0.0136	2.93	0.46	0.0116	2.48	1.87

Wadi ad-Dawasir:

Consistent with the behavior observed for Algodones Dunes, BRDF normalization reduced the overall uncertainty in all bands, with more reduction occurring in the longer wavelength bands. Atmospheric normalization alone appeared to have little effect on the overall uncertainty, not surprising given this is a desert site.

Table 15: TOA Reflectance Summary Statistics for OLI Bands After Atmospheric and BRDF Normalization.

Bands	Before Atmospheric Normalization			After Atmospheric Normalization			Uncertainty After BRDF Normalization (%)
	Mean	STD	Uncertainty (%)	Mean	STD	Uncertainty (%)	
CA	0.21	0.0060	2.89	0.21	0.0060	2.82	2.75
Blue	0.21	0.0065	3.08	0.21	0.0065	2.92	2.81
Green	0.25	0.0060	2.40	0.25	0.0060	2.25	2.08
Red	0.34	0.0071	2.11	0.34	0.0071	2.11	1.68
NIR	0.41	0.0089	2.17	0.41	0.0089	2.17	1.56
SWIR1	0.50	0.0100	2.00	0.50	0.0100	2.00	1.18
SWIR2	0.45	0.0131	2.88	0.45	0.0131	2.72	1.80

CHAPTER 4

Conclusion and Future Directions

A new model was developed to characterize and normalize effects of atmospheric parameters on TOA reflectance, using available ETM+/OLI image data and nearby weather station data acquired for the Algodones Dunes and Wadi-ad-Dawasir sites. Moreover, according to the results presented in Chapter 3, the following observations can be made:

- Atmospheric pressure was found to be significant at shorter wavelengths. This result is not unexpected, as i) Rayleigh scattering at shorter wavelengths is greater, and Rayleigh scattering is a function of atmospheric pressure; and ii) shorter wavelengths are more affected by atmospheric aerosols. For Algodones Dunes, the relationship was positive for the ETM+ Blue and OLI Coastal/Aerosol and Blue bands (increased TOA reflectance at higher atmospheric pressures). For Wadi-ad-Dawasir, the relationship was negative in the OLI Coastal/Aerosol and Blue bands (decreased TOA reflectance at higher atmospheric pressures); for both sites, the relationship was

negative in the OLI Green band. This was a surprising result for the Coastal/Aerosol and Blue bands, suggesting a potential site dependence.

- Also, not surprisingly, water vapor was found to be significant at longer wavelengths, tending to reduce TOA reflectance. This was found to be more of an issue with the ETM+ in the NIR and SWIR1 bands, and with both sensors in the SWIR2 band. Again, this is not unexpected, as it follows from each sensor's observed spectral response.

- In all cases, linear models of atmospheric parameters accounted for less than 50% of the observed variability in TOA reflectance, based on the estimated regression R^2 values. Exponential models for atmospheric pressure accounted for similarly low levels of variability.

- For Algodones Dunes, BRDF normalization after atmospheric normalization reduced the uncertainty to within 2% for all ETM+ bands except SWIR2, whose uncertainty was reduced from approximately 3.5% to approximately 2.7%. Similar normalizations reduced the uncertainty to within 1% for all OLI bands except SWIR2, whose uncertainty was reduced to approximately 2%. For the Wadi ad-Dawasir site, BRDF normalization reduced the uncertainty to within 2% for all OLI bands except the Coastal/Aerosol and Blue bands. However, these figures should be considered tentative pending additional characterization of each site.

4.1 Processing Recommendations

Based on the results obtained from this work, the following processing recommendations can be made:

- Atmospheric parameter measurements should be acquired as close to the image acquisition time as possible.

- Ground stations measuring surface humidity and atmospheric pressure should be as close as possible to the test site.

- Locally accessible databases containing more temporally complete ground station information should be developed.

- To provide maximum reduction in uncertainty, BRDF correction should be performed after atmospheric correction.

4.2 Future Directions

This work could be extended in one or more of the following ways:

- Explore more stable sites throughout the world having nearby weather stations, so that those sites would be useful for calibration purposes.

- Try to characterize the relationship between additional atmospheric parameters and TOA reflectance at shorter wavelengths. Potential parameters for these bands would most likely be those affecting aerosol characteristics, such as wind speed and/or visibility.

- Develop a "composite" model simultaneously accounting for atmospheric and BRDF effects.

References

[1]   D. L. Helder, B. Basnet and D. Morstad, "*Optimized identification of worldwide radiometric   pseudo-invariant calibration sites*," Canadian Journal of Remote Sensing, vol. 36, pp. 527-539.

[2]   D. Helder, J. Thome, N. Mishra, G. Chander, X. Xiong, A. Angal, and T. Choi, "Absolute Calibration of Landsat Using a Pseudo Invariant Calibration Site", *IEEE Trans. Geosci. RemoteSens.,* vol. 51, no. 3, 2013.

[3]   Wayne C. Turner, Steve Doty, "*Energy Management Handbook*", 6th Ed., Lilburn, GA: Fairmont Press, 2007, pp P1-P2.

[4]   A.V. Kozak, V.G. Metlov, G.A. Terez and E.I. Terez, "*On accounting for temperature and pressure in determining the Rayleigh scattering in the earth's atmosphere*", Bulletin of the Crimean Astrophysical Observatory, June 2010, Volume 106, Issue 1, pp 87-91

[5]   M M Farhad, "*Cross calibration and validation of Landsat 8 OLI and Sentinel 2A MSI*", *Masters Graduate Thesis: South Dakota State University,* 2018.

[6]   H. Vuppula, "*Normalization of pseudo-invariant calibration sites for increasing the temporal resolution and long-term trending*", *Masters Graduate Thesis: South Dakota State University,* 2017.

[7]   R. Tabassum, "Worldwide optimal PICS search", *Masters Graduate Thesis: South Dakota State University,* 2017.

[8]   https://landsat.usgs.gov/product-information.

[9]   https://landsat.usgs.gov/using-usgs-landsat-8-product.

[10]   H. Cosnefroy, M. Leroy, and X. Briottet, "*Selection and characterization of Saharan and Arabian desert sites for the calibration of optical satellite sensors*," *Remote Sensing of Environment,* vol. 58, pp. 101-114, 1996.